PCCP

ROYAL SOCIETY OF CHEMISTRY

PAPER

View Article Online
View Journal | View Issue

Cite this: *Phys. Chem. Chem. Phys.*, 2025, **27**, 3230

Thermoelectric properties of the low-spin lanthanide cobalate perovskites $LaCoO_3$, $PrCoO_3$, and $NdCoO_3$ from first-principles calculations†

Alveena Z. Khan, Joseph M. Flitcroft and Jonathan M. Skelton *

An *ab initio* modelling workflow is used to predict the thermoelectric properties and figure of merit *ZT* of the lanthanide cobalates $LaCoO_3$, $PrCoO_3$ and $NdCoO_3$ in the orthorhombic *Pnma* phase with the low-spin magnetic configuration. The $LnCoO_3$ show significantly lower lattice thermal conductivity than the widely-studied $SrTiO_3$, due to lower phonon velocities, with a large component of the heat transport through an intraband tunnelling mechanism characteristic of amorphous materials. Comparison of the calculations to experimental measurements suggests the p-type electrical properties are significantly degraded by the thermal spin crossover, and materials-engineering strategies to suppress this could yield improved *ZT*. We also predict that n-doped $LnCoO_3$ could show larger Seebeck coefficients, superior power factors, lower thermal conductivity, and higher *ZT* than $SrTiO_3$. Our results highlight the exploration of a wider range of perovskite chemistries as a facile route to high-performance oxide thermoelectrics, and identify descriptors that could be used as part of a modelling-based screening approach.

Received 11th November 2024,
Accepted 30th December 2024

DOI: 10.1039/d4cp04303k

rsc.li/pccp

1 Introduction

60–70% of global energy is currently lost as heat, and technologies to improve efficiency are a key enabler of the transition to sustainable energy.[1] Thermoelectric (TE) power, which harnesses the Seebeck effect in a TE material to convert heat to electricity, is a leading contender to address this challenge.[2] The performance of a TE material is typically defined by the dimensionless figure of merit *ZT*:[3]

$$ZT = \frac{S^2\sigma T}{\kappa_{el} + \kappa_{latt}} \quad (1)$$

A large *ZT* requires a high Seebeck coefficient *S* and electrical conductivity σ to optimise the power factor $S^2\sigma$ (PF), and a low combined electronic and lattice thermal conductivity $\kappa = \kappa_{el} + \kappa_{latt}$. The *S*, σ and κ_{el} depend on the electronic structure and the carrier concentration, *n*, such that the σ and κ_{el} are typically proportional to *n* while the *S* is inversely proportional to *n*.[3] The carrier concentration can be optimised with chemical doping, and the largest PFs are usually obtained for heavily-doped semiconductors. The κ_{latt} arises from heat transport through phonons and depends on the material structure and chemical bonding,[4] and low κ_{latt} is often associated with heavy elements, weak bonding, and strong anharmonicity arising from *e.g.* active lone pairs or phase transitions.[4–6]

The majority of current high-performance TE materials are chalcogenides, including: Bi_2Te_3 (*ZT* up to approx. 1.2 from 300–400 K,[7,8] and 1.4 between 400–500 K,[9] in $(Bi,Sb)_2(Se,Te)_3$ alloys); PbTe ($ZT \approx 2.5$ at $T > 900$ K in PbTe—SrTe alloys[10,11]); and SnSe (p-type *ZT* up to 3.1 at 773 K,[12,13] n-type *ZT* up to 2.3 at 873 K[14]). Despite their performance, the current industry standards Bi_2Te_3 and PbTe are unsuitable for widespread application due to the scarcity of Te, which has a lower crustal abundance than Pt, and the environmental toxicity of Pb, which creates issues with end-of-life disposal.[2] Chalcogenides can also be prone to poor thermal stability and oxidation at elevated temperature.[15,16]

Oxide-based TEs are highly desirable for their elemental abundance, high melting temperature and resistance to oxidation, but their *ZT* is often limited by high κ_{latt} and low σ, the latter of which requires a high doping level to offset at the expense of a reduced absolute $|S|$.[17] Nonetheless, reports of large thermoelectric power factors in the 1990s has spurred research into several families of oxide materials. Promising p-type oxides include the layered cobalates $Na_2Co_2O_4$[18–20] ($ZT = 0.92$ at 900 K in $Na_xCo_2O_4$/Ag composites[21]), $Ca_3Co_4O_9$[22] ($ZT = 0.87$ at 973 K in single-crystal $(Ca_2CoO_3)_{0.7}CoO_2$,[23]

Department of Chemistry, University of Manchester, Oxford Road, Manchester M13 9PL, UK. E-mail: jonathan.skelton@manchester.ac.uk

† Electronic supplementary information (ESI) available: Includes additional data on the phonon spectra, lattice thermal conductivity, electrical-transport properties and thermoelectric figure of merit, and comparison of selected calculated properties to experimental measurements, to support the discussion in the text. See DOI: https://doi.org/10.1039/d4cp04303k

ZT = 0.74 at 800 K in polycrystalline $Ca_{3-x}Tb_xCo_4O_9$,[24]) and $Bi_2Sr_2Co_2O_y$[25] (ZT = 0.26 at 973 K in $Bi_2Sr_2Co_2O_y$/Ag composites[26]). Candidate n-type oxides include ZnO[27] (ZT = 0.65 at 1247 K in $Zn_{0.96}Al_{0.02}Ga_{0.02}O$[28]) and the oxide perovskites $SrTiO_3$[29–31] (ZT = 0.66 at 1100 K in $Sr_{0.9}La_{0.1}Ti_{0.9}Nb_{0.1}O_3$[32]) and $CaMnO_3$[33,34] (ZT = 0.67 at 773 K in $Ca_{2.97}Bi_{0.03}MnCu_{0.04}O_{3-\delta}$[35]). However, while perovskites, and in particular STO, have received considerable attention as prospective oxide TEs, they have yet to achieve a ZT competitive with flagship chalcogenide materials.[17]

The lanthanide cobalates $LnCoO_3$ (Ln = La or a rare-earth metal Ce-Lu) are a family of perovskite oxides that, in contrast to the titanates and manganates, typically show p-type conductivity with relatively large Seebeck coefficients around room temperature.[20,36] Reports of n-type lanthanide cobalates are uncommon, but n-type behaviour at low temperature has been observed in several $LnCoO_3$.[37–39] With the exception of $LaCoO_3$, the $LnCoO_3$ typically adopt the low-symmetry orthorhombic *Pnma* perovskite structure.[37,40,41] The octahedral Co^{3+} have a low-spin magnetic arrangement at low temperature but progressively convert to a high-spin configuration at elevated T.[42] This results in a significant increase in the electrical conductivity at high temperature, but at the cost of a large reduction in the Seebeck coefficient.[36–39,43,44] Despite their potentially promising electrical properties, experiments have so far reported maximum $ZT < 0.1$,[36,39,43,44] which are not competitive with more widely-studied perovskite oxides such as $SrTiO_3$.

A recent theoretical study of the lanthanide cobalates $LaCoO_3$ (LCO), $PrCoO_3$ (PCO) and $NdCoO_3$ (NCO) suggested the potential for high-temperature p-type ZT up to $\sim$0.75.[45] However, this study modelled the high-symmetry cubic phases, which are not the ground state,[37,40,41] determined the electrical properties with respect to an unknown relaxation time and without attempting to optimise the carrier concentration, and did not account for the κ_{latt} in the predicted ZT. In this work, we apply a fully *ab initio* workflow for predicting thermoelectric performance, which we have previously shown to yield accurate predictions for the titanate perovskites,[46] to better establish the potential of the $LnCoO_3$ as oxide TEs. We find that the $LnCoO_3$ benefit from a low κ_{latt} and large $|S|$, the latter of which supports heavy doping and large σ and PFs. Comparison to experiments indicates that the electrical properties are severely degraded by the spin transition, and that exploring methods to suppress this may be a fruitful avenue for improving the ZT. More generally, by comparing to similar calculations on the titanate perovskites, including $SrTiO_3$, we identify descriptors that could be indicative of good thermoelectric performance, and which could be used as the basis to explore a wider range of oxide perovskite chemistries.

2 Computational modelling

2.1 Prediction of thermoelectric properties

2.1.1 Lattice thermal conductivity. The contribution to the lattice thermal conductivity from ''particle-like'' heat transport through phonons, $\boldsymbol{\kappa}_p$, was calculated within the single-mode relaxation-time approximation (SM-RTA).[47]

In this model, the macroscopic $\boldsymbol{\kappa}_p$ is an average over contributions $\boldsymbol{\kappa}_{\boldsymbol{q}j}$ from individual phonon modes $\boldsymbol{q}j$, with wavevector $\boldsymbol{q}$ and band index j, according to ref. 47:

$$\boldsymbol{\kappa}_p(T) = \frac{1}{N_{\boldsymbol{q}}V}\sum_{\boldsymbol{q}j}\boldsymbol{\kappa}_{\boldsymbol{q}j} = \frac{1}{N_{\boldsymbol{q}}V}\sum_{\boldsymbol{q}j}C_{\boldsymbol{q}j}(T)\boldsymbol{v}_{\boldsymbol{q}j}\otimes\boldsymbol{v}_{\boldsymbol{q}j}\tau_{\boldsymbol{q}j}(T) \quad (2)$$

The normalisation factor is the product of the unit-cell volume V and the number of wavevectors $N_{\boldsymbol{q}}$ included in the summation. The modal heat capacities $C_{\boldsymbol{q}j}$ are given by:

$$C_{\boldsymbol{q}j}(T) = \sum_{\boldsymbol{q}j}k_B\left[\frac{\hbar\omega_{\boldsymbol{q}j}}{k_BT}\right]^2 n_{\boldsymbol{q}j}(T)\left(n_{\boldsymbol{q}j}(T)+1\right) \quad (3)$$

where $n_{\boldsymbol{q}j}$ are the phonon occupation numbers from the Bose—Einstein distribution:

$$n_{\boldsymbol{q}j}(T) = \frac{1}{\exp\left[\hbar\omega_{\boldsymbol{q}j}/k_BT\right]-1} \quad (4)$$

The mode group velocities $\boldsymbol{\nu}_{\boldsymbol{q}j}$ are given by the gradient of the phonon frequency dispersion:

$$\boldsymbol{v}_{\boldsymbol{q}j} = \frac{\partial\omega_{\boldsymbol{q}j}}{\partial\boldsymbol{q}} \quad (5)$$

Finally, the phonon lifetimes $\tau_{\boldsymbol{q}j}$ are determined from the inverse of the phonon linewidths (scattering rates) $\Gamma_{\boldsymbol{q}j}$:

$$\tau_{\boldsymbol{q}j}(T) = \frac{1}{\Gamma_{\boldsymbol{q}j}(T)} \quad (6)$$

In this work we determine the linewidths using the third-order perturbative method described in ref. 47, in which the $\Gamma_{\boldsymbol{q}j}$ are a sum of contributions from energy- and momentum-conserving three-phonon scattering processes.

In structurally-complex materials with small intraband frequency spacing, and/or in materials with short $\tau_{\boldsymbol{q}j}$ (*i.e.* broad $\Gamma_{\boldsymbol{q}j}$), there may be non-negligible heat conduction through the ''wave-like'' intraband tunnelling characteristic of amorphous materials (glasses).[48] This contribution to the thermal conductivity, $\boldsymbol{\kappa}_w$, can be obtained by solving the Wigner transport equation using the approach outlined in ref. 48. The (total) lattice thermal conductivity is then determined from:

$$\boldsymbol{\kappa}_{latt}(T) = \boldsymbol{\kappa}_p(T) + \boldsymbol{\kappa}_w(T) \quad (7)$$

Finally, we note that the $\boldsymbol{\kappa}_p$, $\boldsymbol{\kappa}_w$ and $\boldsymbol{\kappa}_{latt}$ are 3 × 3 tensors in which the three diagonal elements $\boldsymbol{\kappa}_{\alpha\alpha}$ correspond to transport along the Cartesian directions $\alpha = x$, y and z. Thermoelectric materials are rarely prepared as single crystals, and typically take the form of consolidated powders or thin films with randomly-oriented crystal grains. In this case, the measured (scalar) κ_{latt} can be modelled as the average of the diagonal elements:

$$\kappa = \frac{1}{3}\mathrm{Tr}[\boldsymbol{\kappa}] = \frac{1}{3}\left[\kappa_{xx}+\kappa_{yy}+\kappa_{zz}\right] \quad (8)$$

where Tr denotes the matrix trace. We distinguish the scalar and tensor quantities using Roman and bold type respectively.

2.1.2 Electrical conductivity, Seebeck coefficient and electronic thermal conductivity. The three electrical transport

properties, *viz.* the electrical conductivity $\boldsymbol{\sigma}$, Seebeck coefficient $\boldsymbol{S}$ and electronic thermal conductivity $\boldsymbol{\kappa}_{\mathrm{el}}$, were determined using the approach outlined in ref. 49 and 50.

The spectral conductivity $\boldsymbol{\Sigma}$ and generalised moments of the transport distribution function $\boldsymbol{L}^n$ are calculated according to:[49,50]

$$\boldsymbol{\Sigma}(\varepsilon, T) = \sum_j \int \frac{1}{8\pi^3} \boldsymbol{v}_{kj} \otimes \boldsymbol{v}_{kj} \tau_{kj}(T) \delta\left[\varepsilon - \varepsilon_{kj}\right] \mathrm{d}\boldsymbol{k} \tag{9}$$

$$\boldsymbol{L}^n(\varepsilon_{\mathrm{F}}, T) = e^2 \int \left(\boldsymbol{\Sigma}(\varepsilon, T)(\varepsilon - \varepsilon_{\mathrm{F}})^n \left[-\frac{\partial f^0(\varepsilon, \varepsilon_{\mathrm{F}}, T)}{\partial \varepsilon} \right] \mathrm{d}\varepsilon \right) \tag{10}$$

In a similar manner to the $\boldsymbol{\kappa}_{\mathrm{latt}}$, the integrals in eqn (9) and (10) are performed over electronic states $\boldsymbol{kj}$ with electron wavevector $\boldsymbol{k}$ and band index j. e is the elementary charge. $\varepsilon_{\boldsymbol{kj}}$ are the electron band energies and $f^0(\varepsilon, \varepsilon_{\mathrm{F}}\ T)$ is the Fermi—Dirac distribution function given by:

$$f^0(\varepsilon, \varepsilon_{\mathrm{F}}, T) = \frac{1}{\exp[(\varepsilon - \varepsilon_{\mathrm{F}})/k_{\mathrm{B}}T] + 1} \tag{11}$$

where ε_{F} is the Fermi energy and k_{B} is the Boltzmann constant. The electron group velocities $\boldsymbol{\nu}_{\boldsymbol{kj}}$ are calculated from (*cf.* eqn (5)):

$$\boldsymbol{v}_{kj} = \frac{\partial \varepsilon_{kj}}{\partial \boldsymbol{k}} \tag{12}$$

The electron lifetimes $\tau_{\boldsymbol{kj}}$ are obtained by estimating the electron scattering rates from acoustic deformation potential (ADP), polar-optic phonon (POP), ionised impurity (IMP) and piezoelectric (PIE) scattering within the momentum relaxation-time approximation (MRTA):[50]

$$\tau_{\boldsymbol{kj}}^{-1}(T) = \Gamma_{\boldsymbol{kj}}^{\mathrm{ADP}}(T) + \Gamma_{\boldsymbol{kj}}^{\mathrm{POP}}(T) + \Gamma_{\boldsymbol{kj}}^{\mathrm{IMP}}(T) + \Gamma_{\boldsymbol{kj}}^{\mathrm{PIE}}(T) \tag{13}$$

Expressions for the scattering rates and matrix elements can be found in ref. 50.

Once the $\boldsymbol{L}^n(T)$ have been calculated, the $\boldsymbol{\sigma}$, $\boldsymbol{S}$ and $\boldsymbol{\kappa}_{\mathrm{el}}$ can be determined from:[49,50]

$$\boldsymbol{\sigma}(\varepsilon_{\mathrm{F}}, T) = \boldsymbol{L}^0(\varepsilon_{\mathrm{F}}, T) \tag{14}$$

$$\boldsymbol{S}(\varepsilon_{\mathrm{F}}, T) = \frac{1}{eT} \frac{\boldsymbol{L}^1(\varepsilon_{\mathrm{F}}, T)}{\boldsymbol{L}^0(\varepsilon_{\mathrm{F}}, T)} \tag{15}$$

$$\boldsymbol{\kappa}_{\mathrm{el}}(\varepsilon_{\mathrm{F}}, T) = \frac{1}{e^2 T} \left[\frac{\left(\boldsymbol{L}^1(\varepsilon_{\mathrm{F}}, T)\right)^2}{\boldsymbol{L}^0(\varepsilon_{\mathrm{F}}, T)} - \boldsymbol{L}^2(\varepsilon_{\mathrm{F}}, T) \right] \tag{16}$$

We note that the $\boldsymbol{L}^n$, and hence the $\boldsymbol{\sigma}$, $\boldsymbol{S}$ and $\boldsymbol{\kappa}_{\mathrm{el}}$, depend on the Fermi energy. This can be adjusted to specify an extrinsic carrier concentration (''doping level'') n, under the assumption that the doping does not significantly affect the host band structure. This is termed the ''rigid band approximation'' (RBA).

We also note that, while we do not do so in this work, a common approximation used in electronic transport calculations is to replace the $\tau_{\boldsymbol{kj}}$ with a (possibly temperature-dependent) constant value τ_{el}.[49] In this case, the $\boldsymbol{\sigma}$ and $\boldsymbol{\kappa}_{\mathrm{el}}$ are linearly proportional to the τ_{el} and the $\boldsymbol{S}$, which is the ratio of two $\boldsymbol{L}^n$ (*cf.* eqn (15)), is independent of the lifetime.

Finally, as for the $\boldsymbol{\kappa}_{\mathrm{latt}}$, the $\boldsymbol{\sigma}$, $\boldsymbol{S}$ and $\boldsymbol{\kappa}_{\mathrm{el}}$ are 3×3 tensors, and scalar averages σ, S and κ_{el} can be obtained in an analogous manner to eqn (8). The power factor $S^2\sigma$ in eqn (1) is also orientation dependent, and the PF along a given Cartesian direction can be calculated from:

$$(S^2\sigma)_\alpha = {S_{\alpha\alpha}}^2 \sigma_{\alpha\alpha} \tag{17}$$

The scalar average PF is obtained in the same way, using the averaged S and σ.

2.1.3 Thermoelectric figure of merit. Finally, the calculated $\boldsymbol{\kappa}_{\mathrm{latt}}$ and $\boldsymbol{\sigma}$, $\boldsymbol{S}$ and $\boldsymbol{\kappa}_{\mathrm{el}}$ can be combined to determine the thermoelectric figure of merit ZT using eqn (1). The $\boldsymbol{\kappa}_{\mathrm{latt}}$ is a function of temperature, while the three electrical properties are a function of both T and the Fermi energy ε_{F} (extrinsic carrier concentration n; *cf.* eqn (7) and (14)–(16)). We therefore determine the ZT as a function of both T and n.

The ZT is orientation dependent and the values along the three Cartesian directions can be calculated as:

$$(ZT)_\alpha = \frac{{S_{\alpha\alpha}}^2 \sigma_{\alpha\alpha} T}{\kappa_{\mathrm{el},\alpha\alpha} + \kappa_{\mathrm{latt},\alpha\alpha}} \tag{18}$$

As for the power factor, the scalar average ZT is calculated using the scalar averages of the four constituent properties.

2.2 Density-functional theory calculations

Calculations were performed using pseudopotential plane wave density functional theory (DFT) as implemented in the Vienna *Ab initio* Simulation Package (VASP) code.[51]

Initial structures of $LaCoO_3$ (LCO), $PrCoO_3$ (PCO) and $NdCoO_3$ (NCO) in the orthorhombic *Pnma* space group were taken from the Materials Project (MP) database[52] (mp-1185232, mp-20090, mp-22599) and optimised to tight tolerances of 10^{-8} eV on the total energy and 10^{-3} eV Å^{-1} on the forces.

Electron exchange and correlation were modelled using the PBEsol generalised-gradient approximation (GGA) functional.[53] The ion cores were modelled using projector-augmented wave pseudopotentials (PAW PPs).[54,55] For La, Co and O, we used PPs with the valence configurations: La – $5s^2\ 5p^6\ 6s^2\ 5d^1$; Co – $4s^1\ 3d^8$ and O – $2s^2\ 2p^4$. For Pr and Nd we used the Ln^{3+} PPs, which place two/three f electrons for Pr^{3+}/Nd^{3+} in the pseudopotential core, resulting in the same valence configuration as the La PP. The valence wavefunctions were described using a plane-wave basis with an 800 eV kinetic-energy cutoff, and the electronic Brillouin zones were sampled using Γ-centred Monkhorst—Pack $\boldsymbol{k}$-point meshes[56] with $3 \times 3 \times 2$ subdivisions. These parameters were chosen based on explicit testing to converge the absolute total energies to <1 meV atom^{-1} and the external pressure to <1 kbar (0.1 GPa).

2.2.1 Lattice dynamics and thermal conductivity. Lattice-dynamics and thermal-conductivity calculations were performed using the supercell finite-differences approach implemented in the Phonopy and Phono3py codes.[47,57] The second-order (harmonic) force constants were computed in $3 \times 2 \times 3$ expansions of the primitive cells with 360 atoms. Atom-projected phonon density of states (PDoS) curves were computed by interpolating the phonon frequencies onto regular Γ-centred $\boldsymbol{q}$-point grids with

12 × 12 × 12 subdivisions and using the linear tetrahedron method for Brillouin-zone integration. Phonon dispersions were obtained by evaluating the frequencies at strings of $\boldsymbol{q}$ points passing through the high-symmetry points in the *Pnma* Brillouin zone. Non-analytical corrections to the dynamical matrices at $\boldsymbol{q} \rightarrow \Gamma$ were included using the approach in ref. 58, with Born effective-charge tensors $\boldsymbol{Z}^*$ and high-frequency dielectric constants $\boldsymbol{\varepsilon}_\infty$ computed using the density-functional perturbation theory (DFPT) routines in VASP.[59]

The third-order (anharmonic) force constants were computed in 2 × 1 × 2 expansions of the conventional cells (80 atoms). The "particle-like" lattice thermal conductivities for band transport were calculated using the single mode relaxation time approximation (SM-RTA) to the phonon Boltzmann transport equation by combining the second- and third-order force constants to obtain modal heat capacities $C_{\boldsymbol{q}j}$, group velocities $\boldsymbol{\nu}_{\boldsymbol{q}j}$ and lifetimes $\tau_{\boldsymbol{q}j}$ on uniform Γ-centred 8 × 8 × 8 $\boldsymbol{q}$-point sampling meshes. This mesh was chosen based on explicit testing to converge the scalar average of the $\boldsymbol{\kappa}_\mathrm{p}$ tensors (eqn (2) and (8)) to within 5% of the values obtained with larger sampling meshes. We also solved the Wigner transport equation for the converged meshes to determine the $\boldsymbol{\kappa}_\mathrm{w}$ contribution from intraband tunnelling.[48]

2.2.2 Electronic transport. Electronic transport calculations were performed using the AMSET code.[50] Accurate band gaps E_g were obtained using the HSE06 hybrid functional.[60] These calculations were also used to obtain electronic PDoS curves using a Gaussian smearing with a width σ = 0.01 eV. Uniform band-structure calculations were then performed with PBEsol and denser 6 × 6 × 4 $\boldsymbol{k}$-point meshes, and the bandgaps increased to the HSE06 values using a scissors operator. These meshes were further interpolated to a ∼30× higher density when calculating the transport properties. The charge densities from the calculations were also used to calculate the band energies at strings of $\boldsymbol{k}$-points along the high-symmetry paths in the *Pnma* Brillouin zone, which were similarly corrected using scissors operators, to obtain electronic band structures. The combined band structure and PDoS curves were plotted using sumo.[61]

AMSET estimates the electronic relaxation times by summing scattering rates from four different processes, *viz.* acoustic deformation potential (ADP), polar optic phonon (POP), piezoelectric (PIE), and ionised impurity (IMP) scattering (eqn (13)), requiring a range of material properties to be calculated.

Deformation potentials were computed by performing a series of single-point energy calculations on deformed structures, generated using AMSET, with PBEsol.

High-frequency dielectric constants $\boldsymbol{\varepsilon}_\infty$ were obtained using the linear-optics routines in VASP[59] and non-self-consistent HSE06,[60,62] where the electronic band energies are evaluated using PBE Kohn—Sham wavefunctions without updating the electron orbitals. The ionic contributions to the dielectric constants $\boldsymbol{\varepsilon}_\mathrm{ionic}$, Born effective charges $\boldsymbol{Z}^*$ and piezoelectric moduli $\boldsymbol{e}^{(0)}$ were determined using DFPT with PBEsol.[59] The $\boldsymbol{\varepsilon}_\infty$ and $\boldsymbol{\varepsilon}_\mathrm{ionic}$ were used to obtain the static dielectric constants $\boldsymbol{\varepsilon}_\mathrm{s} = \boldsymbol{\varepsilon}_\infty + \boldsymbol{\varepsilon}_\mathrm{ionic}$. The $\boldsymbol{Z}^*$ were used with the phonon modes at $\boldsymbol{q} = \Gamma$, evaluated with Phonopy, to calculate the polar optic phonon (POP) frequency ω_po. For both the linear-optics and DFPT calculations, convergence tests indicated that 3 × denser $\boldsymbol{k}$-point sampling along each reciprocal-lattice vector, relative to the "base" meshes used for geometry optimisation, was required for convergence.

Finally, the elastic constants C_{ij} were computed using PBEsol and the finite-differences routines in VASP (denser $\boldsymbol{k}$-point sampling was not required for these calculations).

PIE scattering is not relevant to these systems, as the *Pnma* spacegroup is centrosymmetric and the piezoelectric moduli vanish, so we did not include this mechanism when estimating the scattering rates.

3 Results and discussion

3.1 Structure, phonon spectra and lattice thermal conductivity

The optimised structures of the three $LnCoO_3$ are shown in Fig. 1. For PCO and NCO, the lattice parameters are in excellent agreement with experimental measurements, with maximum deviations of 0.8% in the lattice parameters and 1.2% in the unit-cell volume (Table S1, ESI†). For LCO, the Materials Project[52] predicts the *Pnma* structure to be a low-lying metastable phase to the ground-state $R\bar{3}c$ phase,[37] but our optimised lattice parameters and volume differ by up to 5.4% and 10.8%

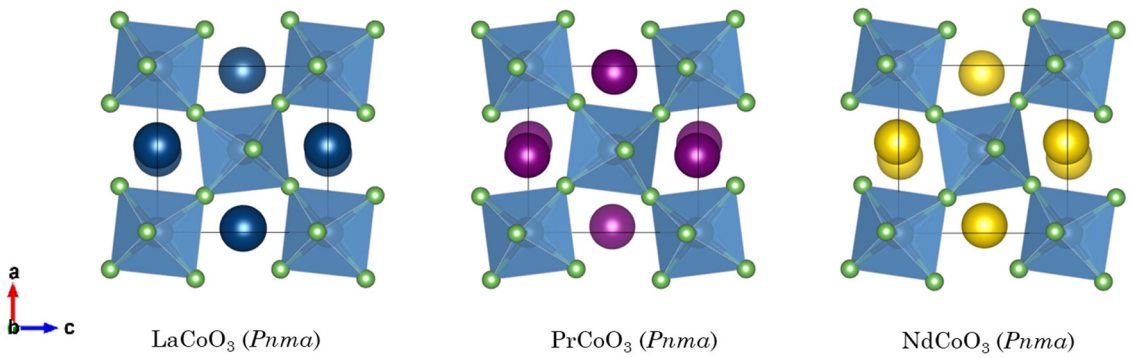

Fig. 1 Optimised structures of $LaCoO_3$, $PrCoO_3$ and $NdCoO_3$ viewed along the crystallographic *b* direction. The Ln atoms are shown in dark blue, purple and yellow, the Co atoms are shown in light blue, and the O atoms are shown in green. These images were prepared using the VESTA software.[63]

from those reported with ref. 37 (ICSD: 164459). However, it is not clear how this *Pnma* structure was obtained, and we are therefore unsure of the origin of this discrepancy.

The calculated phonon spectra of the three $LnCoO_3$ are shown in Fig. 2 and Fig. S1/S2 (ESI†). The phonon spectra are broadly similar, as expected given the chemical similarity of La, Pr and Nd, with the exception that some of the higher-frequency modes of LCO and PCO show shallower dispersion and sharper features in the density of states (DoS) compared to NCO. The DoS curves of all three $LnCoO_3$ show low- and mid/high-frequency groups of modes separated by a small "phonon bandgap". The atom-projected DoS (PDoS) shows that modes in the low-frequency group are predominantly associated with motion of the Ln atoms, while the mid/high-frequency group corresponds to motion of the Co and O atoms, with Co and O making the largest contribution to the mid- and high-frequency modes, respectively. The form of the (P)DoS can therefore largely be explained by the difference in mass between the Ln, Co and O atoms. Finally, the calculated dispersions are free from imaginary modes, indicating all three $LnCoO_3$ to be dynamically stable in the *Pnma* phase.

Turning now to the lattice thermal conductivity, the scalar-average "particle-like" conductivity, κ_p, of the three $LnCoO_3$ are compared in Fig. 3(a). The κ_p is obtained by solving the Boltzmann transport equation for phonons, under the assumption that energy is carried by phonon quasiparticles, and, in most crystalline materials, is the dominant contributor to the κ_{latt}.[47]

At $T = 1000$ K, we predict values of $\kappa_p = 0.66$–0.94 W m^{-1} K^{-1}, which are comparable at the higher end to our previous calculations on orthorhombic $CaTiO_3$ (CTO, $\kappa_p = 0.93$ W m^{-1} K^{-1}) and 30–50% smaller than we predicted for tetragonal $SrTiO_3$ (STO, 1.4 W m^{-1} K^{-1}).[46] The κ_p are generally smallest along the *b* axis and largest along the *c* axis, but the anisotropy is small, with the axial conductivity differing by $<10\%$ of the scalar averages (Table S2, ESI†).

To establish the origin of the differences in the thermal transport, we used the analysis developed in our previous work[4] and determined weighted-average lifetimes, τ_{ph}, such that the κ_p can be written (*cf.* eqn (2)):

$$\begin{aligned}\kappa_p(T) &= \tau_{ph}(T) \times \frac{1}{N_{\boldsymbol{q}} V} \sum_{\boldsymbol{q}j} \frac{\kappa_{\boldsymbol{q}j}(T)}{\tau_{\boldsymbol{q}j}(T)} \\ &= \tau_{ph}(T) \times \frac{1}{N_{\boldsymbol{q}} V} \sum_{\boldsymbol{q}j} C_{\boldsymbol{q}j}(T) \frac{1}{3} \mathrm{Tr}\left[\boldsymbol{v}_{\boldsymbol{q}j} \otimes \boldsymbol{v}_{\boldsymbol{q}j}\right]\end{aligned} \tag{19}$$

where we have taken the scalar average of the group velocity outer product (*cf.* eqn (8)).

The summation on the right-hand side, κ_p/τ_{ph}, is a useful metric for comparing differences in the group velocities, and saturates at high-temperature as the $C_{\boldsymbol{q}j}$ tend to the Dulong–Petit limit. Comparing the κ_p/τ_{ph} of the three $LnCoO_3$ to those of CTO and STO[46] shows that the $LnCoO_3$ have much lower group velocities (Fig. 3(b) and Table S3, ESI†). While the difference to STO may be partly due to the lower-symmetry orthorhombic structure,[4] the fact that the values are 55–60% lower than the isostructural CTO likely indicates weaker chemical bonding compared to the titanate perovskites. A potential explanation for this is the weaker electrostatic interactions in the BO_6 octahedra with Co^{3+} compared to Ti^{4+}. On the other hand, we calculate $\tau_{ph} = 0.38$–0.58 for the three $LnCoO_3$ at $T = 1000$ K, which are 1.6–2.4× longer than CTO and 2.4–4.5× longer than STO (Fig. 3(c) and Table S3, ESI†). It is also of note that the differences in the κ_p among the $LnCoO_3$ are primarily due to differences in the τ_{ph} (*cf.* Fig. 3(a) and (c)). At $T = 1000$ K, NCO and LCO have the largest and smallest κ_p, respectively, which is due to NCO having a 1.7% smaller κ_p/τ_{ph} but a 1.5× longer τ_{ph} (Table S3, ESI†).

In materials where "dense" phonon dispersion curves and small intraband spacing, and/or broad linewidths due to short τ_{ph}, lead to substantial energy overlap between phonon modes, there may be a significant "wave-like" intraband tunnelling contribution, κ_w, to the overall κ_{latt}.[48] Intraband tunnelling is typically the dominant heat-transport mechanisms in amorphous materials (glasses), and can be evaluated by solving the Wigner transport equation. We obtain values of $\kappa_w = 0.55$–0.6 W m^{-1} K^{-1} for the

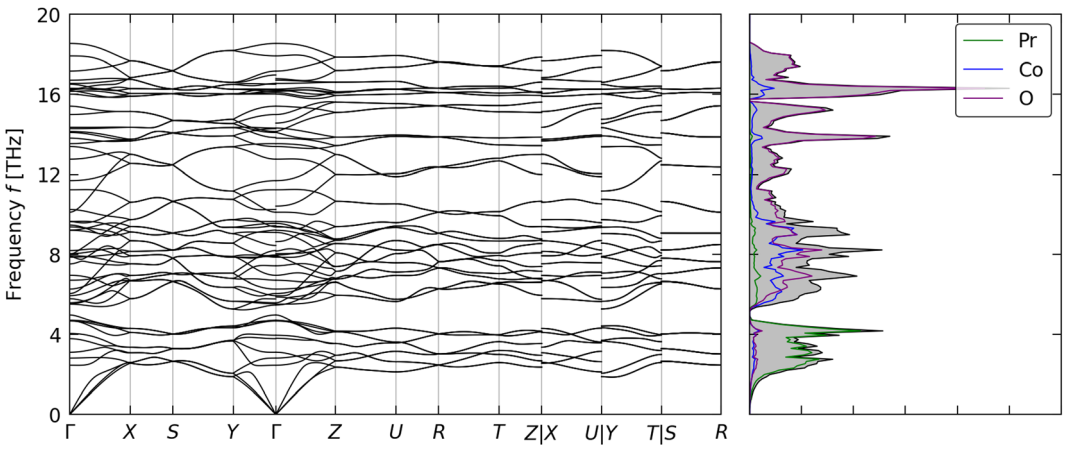

Fig. 2 Phonon dispersion and density of states (DoS) of $PrCoO_3$. The DoS curve shows the total DoS in black/grey with the projections onto the Pr, Co and O atoms in green, blue and purple respectively.

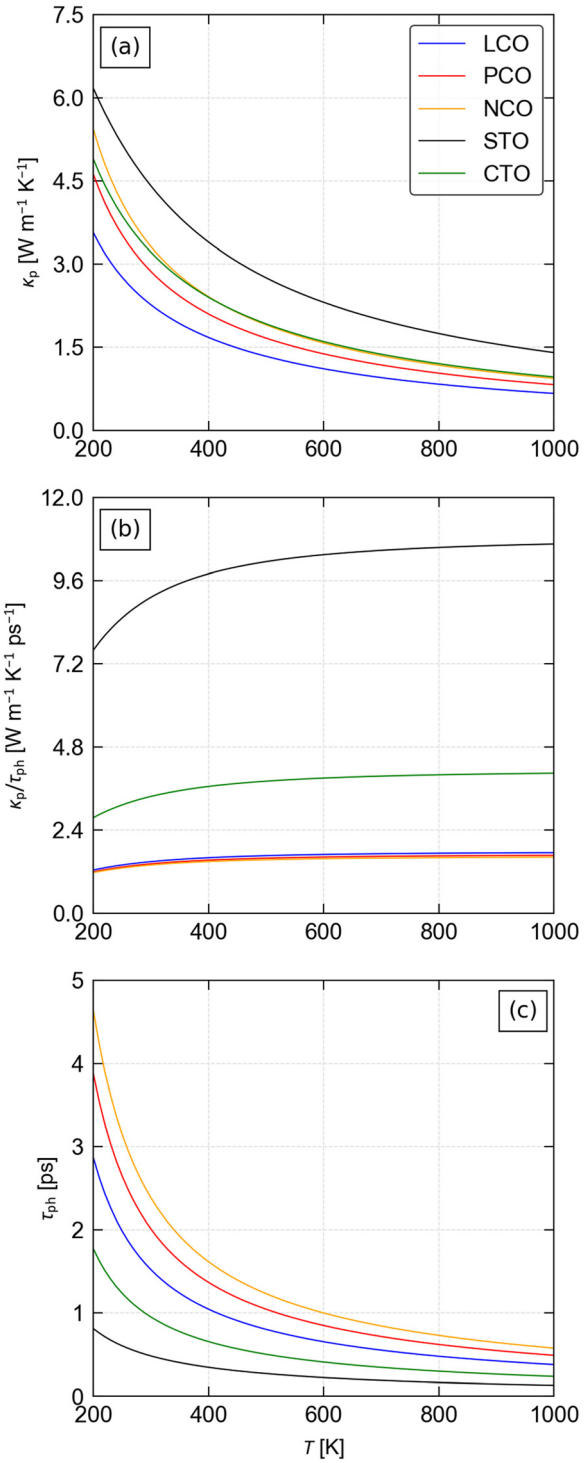

Fig. 3 Analysis of the "particle-like" (band) contribution κ_p to the averaged lattice thermal conductivity κ_{latt} of $LaCoO_3$ (LCO), $PrCoO_3$ (PCO) and $NdCoO_3$ (NCO) using the model developed in our previous work (eqn (19)).[4] The κ_p is written as a the product of a harmonic term κ/τ_{ph}, which at high temperature reflects differences in the phonon group velocities, and a weighted-average lifetime τ_{ph}. Data for $SrTiO_3$ (STO) and $CaTiO_3$ (CTO) from our previous work[46] are shown for comparison.

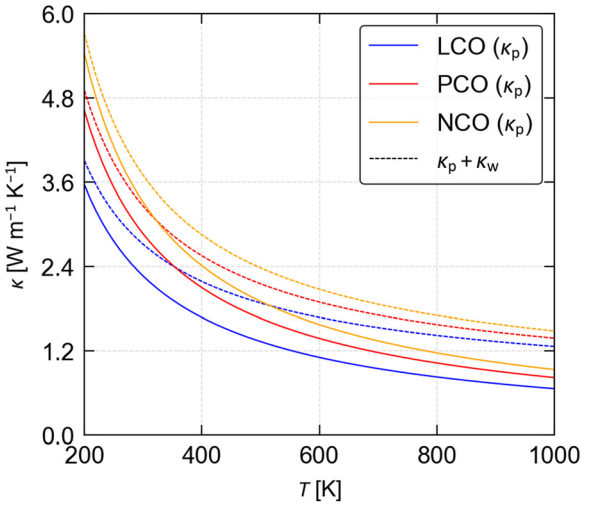

Fig. 4 Contribution to the averaged lattice thermal conductivity κ_{latt} of $LaCoO_3$ (LCO), $PrCoO_3$ (PCO) and $NdCoO_3$ (NCO) from "particle-like" (band) transport κ_p and "wave-like" (intraband tunnelling) transport κ_w as a function of temperature.

three $LnCoO_3$, equal to ~79–90% of the κ_p, which substantially increase the total κ_{latt} to 1.27–1.49 W m^{-1} K^{-1} compared to the κ_p (Fig. 4 and Table S2, ESI†). This indicates that a large proportion of the heat transport in the three $LnCoO_3$ is through this glass-like conduction mechanism. While perhaps surprising, our predicted (total) κ_{latt} of 1.42 W m^{-1} K^{-1} for LCO at 800 K, and 1.49 and 1.61 W m^{-1} K^{-1} for PCO and NCO at 875 K, are reasonable matches to the measured values of 1.75 W m^{-1} K^{-1} for LCO[44] and 1.25 W m^{-1} K^{-1} for PCO/NCO.[43] (We tentatively attribute the underestimated κ_{latt} of LCO to our modelling the metastable *Pnma* rather than the higher-symmetry $R\bar{3}c$ phase, and the overestimated κ_{latt} of PCO and NCO to the morphology of the experimental samples and/or to differences in composition.)

In our previous calculations on the titanate perovskites[46] we determined the κ_p using the same approach as in the present study, but we did not account for intraband tunnelling. To investigate whether this makes a significant contribution to the κ_{latt} of the titanates, we solved the Wigner transport equation for STO and CTO to calculate the κ_w (Fig. S3/S4 and Table S4, ESI†). At T = 1000 K, the κ_w for CTO is 1.6× larger than the κ_p, whereas for STO the κ_w and κ_p are approximately equal and intraband tunnelling increases the predicted κ_{latt} by almost a factor of two. We obtain total thermal conductivities of 2.47 and 2.73 W m^{-1} K^{-1} for CTO and STO, which are a much better match to the experimental measurements of 3.25 and ~3–3.2 W m^{-1} K^{-1} (ref. 64–67) than the κ_p. While the calculations still underestimate the measured values, the discrepancy is on the order of 10–20%, which could easily be ascribed to, for example, incomplete separation of the lattice and electronic contributions to the total thermal conductivity κ or to the presence of (thermally-)conductive impurities.

This leads to the important result that intraband tunnelling likely makes a substantial contribution to the κ_{latt} of the oxide perovskites, and it is necessary to solve the Wigner transport equation, rather than the more usual phonon Boltzmann transport equation, for these systems.[48,57]

3.2 Electronic structure and transport properties

The electronic band structure and density of states (DoS) of the three $LnCoO_3$ are shown in Fig. 5 and Fig. S5/S6 (ESI†). In all three $LnCoO_3$, the valence-band edge is formed of a roughly equal mix of Co 3d and O 2p states, while the conduction-band edge is primarily composed of Co states. Using the HSE06 hybrid functional, we predict indirect bandgaps E_g of between 2.59 eV for LCO and 2.87 eV for NCO, which are considerably larger than the predicted E_g in ref. 45 but consistent with the upper range of values measured in experiments (Table S5, ESI†). For all three $LnCoO_3$ the valence-band maxima (VBM) lie along the $\Gamma \rightarrow Z$ path and the conduction-band minima (CBM) are close to U (Fig. 5 and Fig. S5/S6, ESI†).

Fig. 6 shows the predicted average electrical conductivity σ, absolute Seebeck coefficient $|S|$, power factor $S^2\sigma$ (PF) and electronic thermal conductivity κ_{el} of the three $LnCoO_3$, with both p-type (hole) and n-type (electron) doping, as a function of doping level n at a fixed T = 1000 K.

As for the titanate perovskites,[46] we predict that high doping levels of $n > 10^{20}$ cm^{-3} are required to obtain reasonable σ (Fig. 6(a)). Whereas most experiments on the $LnCoO_3$ have examined p-type doping,[37,39,43,44] our calculations predict that much larger σ can potentially be obtained with n-type doping. Taking $n = 5 \times 10^{21}$ cm^{-3} as a reference point, we predict that the n-type σ = 439–494 S cm^{-1} could be up to $\sim$6$\times$ larger than the p-type σ = 80–85 S cm^{-1} at T = 1000 K. Of the three titanate perovskites $CaTiO_3$, $SrTiO_3$ and $BaTiO_3$ examined in our previous work,[46] we predicted n-type STO to show the most favourable electrical properties. Compared to the three $LnCoO_3$, STO shows a larger σ at $n \approx 10^{20}$ cm^{-3} and above, with a predicted 2.6 $\times$ larger σ = 1268 S cm^{-1} at $n = 5 \times 10^{21}$ cm^{-3}.

The $|S|$ are predicted to decrease monotonically from a relatively large value of around 900 μV K^{-1} to approx. 150 μV K^{-1} over the range of $n = 10^{16}$–10^{22} cm^{-3} tested in our calculations (Fig. 6(b)). Unlike the electrical conductivities, we predict similar $|S|$ for both p- and n-type doping, and we predict a near-constant increase of around 100 μV K^{-1} compared to n-type STO.[46]

The σ and $|S|$ are related to the n and the carrier effective masses m^* according to:[68,69]

$$\sigma = ne\mu = ne \times \frac{(e\tau)}{m_\sigma^*} \tag{20}$$

$$S = \frac{8\pi^2 k_B^2}{3qh^2} m_S^* \left(\frac{\pi}{3n}\right)^{2/3} \tag{21}$$

where $q = \pm e$ for hole and electron carriers, m_σ^* and m_S^* are the conductivity and Seebeck effective masses, respectively, and we have omitted the temperature dependence of the various parameters for brevity. We estimated the m_σ^* and m_S^* for a reference $n = 5 \times 10^{21}$ cm^{-3} and T = 1000 K using the procedure outlined in ref. 69, with a constant electron lifetime of $\tau_{kj} = \tau_{el} = 10^{-14}$ s (Table S6, ESI,† *cf.* eqn (9)). We obtain $m_\sigma^* = 8.07$–$9.28\ m_e$ and $m_S^* = 6.6$–$7.3\ m_e$ for p-type doping, and $m_\sigma^* = 2.26$–$2.6\ m_e$ and $m_S^* = 5.27$–$5.74\ m_e$ for n-type doping. The 3–4$\times$ larger m_σ^* with p-type doping accounts for the majority of the $\sim$6$\times$ higher σ predicted for n-type doping, but indicates that stronger hole carrier scattering must also play a significant role. Similar calculations on n-type STO, with a more appropriate $n = 10^{21}$ cm^{-3}, yield $m_\sigma^* = 0.79$ and $m_S^* = 2.46$, which qualitatively explain the higher σ and lower $|S|$ compared to the three $LnCoO_3$.

The band structures of all three $LnCoO_3$ show low-energy secondary band extrema (VBM/CBM) that could be beneficial to the electrical properties (Fig. 5 and Fig. S5/S6, ESI†). To test this, we also computed the Fermi surface complexity factors $(N_V^* K^*)$ defined in ref. 69:

$$(N_V^* K^*) = \left(\frac{m_S^*}{m_\sigma^*}\right)^{3/2} \tag{22}$$

where N_V^* and K^* are an effective valley degeneracy and effective anisotropy factor, respectively. The calculated $(N_V^* K^*)$ as a function of n and T for the three $LnCoO_3$, for both p- and n-type doping, are shown in Fig. S7–S9 (ESI†). Across the three $LnCoO_3$ we obtain values between 0.3–5.1 and 2.4–9.1 for p- and n-type doping, respectively, which are modest in comparison to

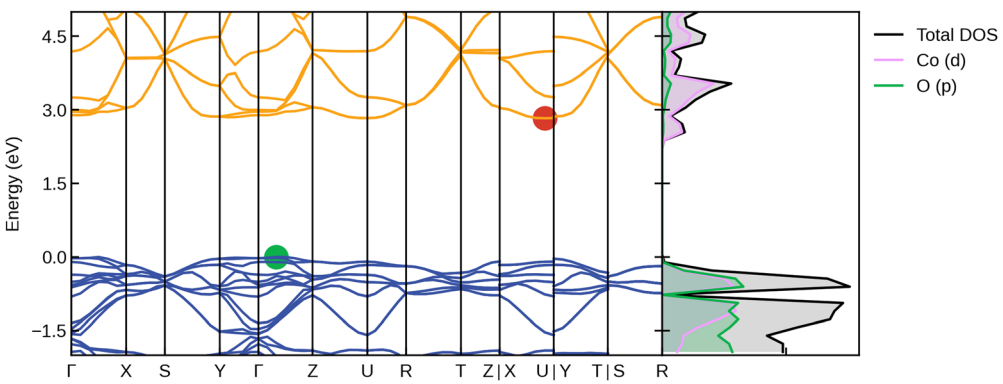

Fig. 5 Calculated electronic band structure and atom-projected density of states (PDoS) of $LaCoO_3$. In the band structure, the valence and conduction bands are shown in blue and orange, and the green and red markers show the positions of the valence-band maximum and conduction-band minimum. In the DoS plot, the total DoS is shown in black and the projections onto the Co d and O p states are shown in purple and green. This plot was generated using sumo.[61]

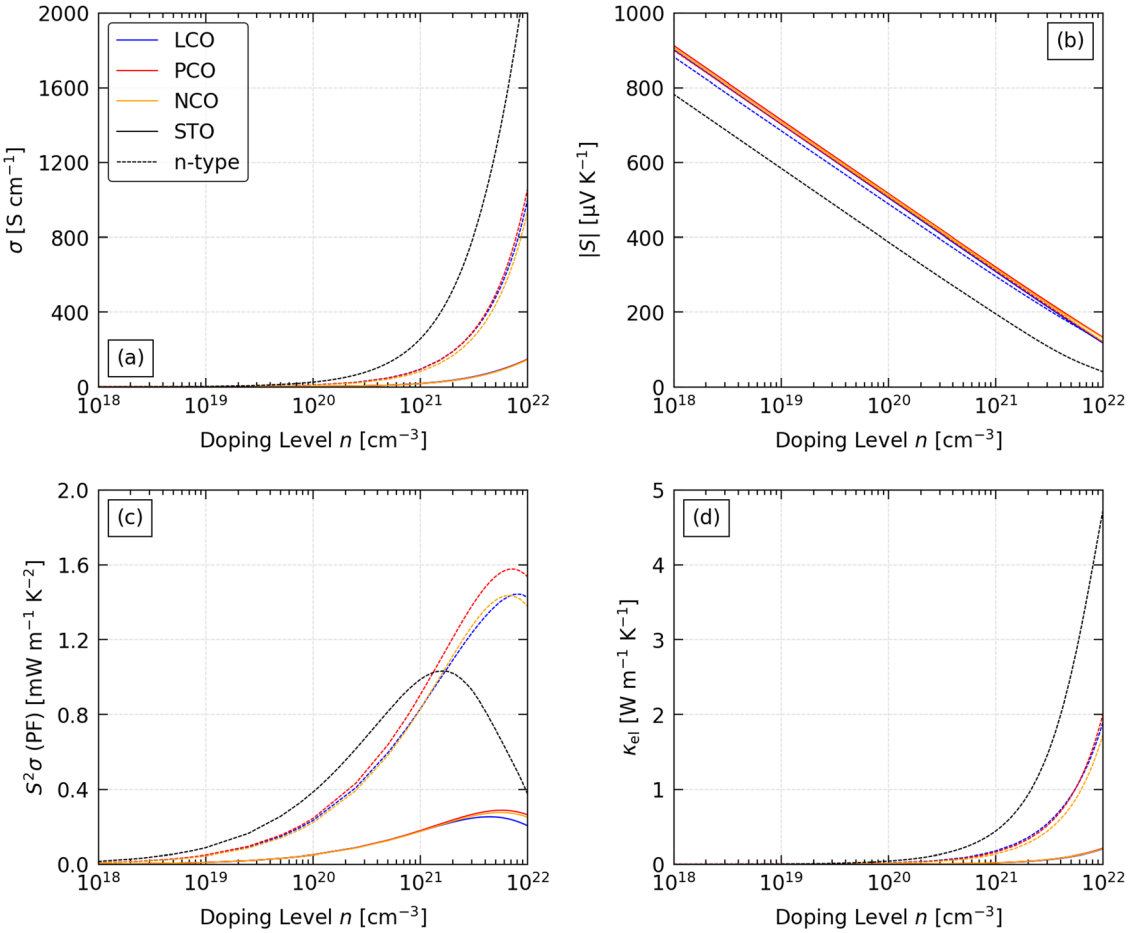

Fig. 6 Predicted electrical properties of $LaCoO_3$ (LCO), $PrCoO_3$ (PCO) and $NdCoO_3$ (NCO) as a function of extrinsic carrier concentration n ("doping level") at a fixed temperature T = 1000 K: (a) electrical conductivity σ, (b) absolute Seebeck coefficient $|S|$, (c) power factor $S^2\sigma$(PF), and (d) electronic thermal conductivity κ_{el}. For all four quantities we show the scalar averages (*cf.* eqn (8) and (17)). Data for n-type $SrTiO_3$ (STO) from our previous work is also shown for comparison.[46]

high-performance chalcogenide thermoelectrics such as GeTe ($(N_V^* K^*) = 49$ at the estimated n that maximises the PF) and PbSe (22).[69] This suggests that, despite the multivalley electronic structure, Fermi surface complexity plays a minor role in the electrical properties of the $LnCoO_3$, although it likely does contribute to the superior n-type transport.

The rise in σ and decrease in $|S|$ with n results in peak PFs between $n = 10^{21}$–10^{22} cm^{-3} (Fig. 6(c)). The predicted maximum PFs for the p- and n-type $LnCoO_3$, and for n-type STO,[46] at T = 1000 K are listed together with the associated n, σ and $|S|$ in Table S7 (ESI†). The p-type PFs range from 0.25–0.29 mW m^{-1} K^{-2} (n = 5–7 × 10^{21} cm^{-3}), while the n-type PFs range from 1.4–1.6 mW m^{-1} K^{-2} (n = 6.5–8 × 10^{21} cm^{-3}). In almost all cases, the maximum and minimum PFs are along the b and c axes, respectively, and align with the respective minimum and maximum in the κ_{latt} (Table S8, ESI†). The anisotropy in the PFs is considerably larger than in the thermal conductivity, and the axial values differ from the averages by up to 25%.

Compared to our previous calculations on the titanate perovskites, we predict comparable n-type PFs to STO at the optimum $n = 2 \times 10^{21}$ cm^{-3} for this system, and considerably higher peak PFs at larger n, because the larger $|S|$ allows the doping level to be increased to offset the lower σ. At T = 1000 K, the largest n-type $S^2\sigma$ = 1.6 mW m^{-1} K^{-1} for PCO (n = 7 × 10^{21} cm^{-3}, S = −149 μV K^{-1}, σ = 712 S cm^{-1}) is 55% larger than the highest $S^2\sigma$ = 1 mW m^{-1} K^{-2} predicted for STO (n = 2 × 10^{21} cm^{-3}, S = −139 μV K^{-1}, σ = 524 S cm^{-1}).

At large n the predicted κ_{el} follow the Widemann–Franz Law:

$$\kappa_{el} = L\sigma T \quad (23)$$

where L is the Lorentz number, which may vary with n and T. As a result of this proportionality, the κ_{el} rise sharply with n (Fig. 6(d)). The low σ of the p-type systems means that the κ_{el} remains an order of magnitude smaller than the κ_{latt} even at large n (*cf.* Fig. 4). On the other hand, we predict much larger κ_{el} = 1–2 W m^{-1} K^{-1} for the n-doped materials, which suggests that the optimum high-T figure of merit will occur at a lower n than the optimum PFs (*cf.* eqn (1)).

The predicted temperature dependence of the σ, $|S|$, PF and κ_{el} of the $LnCoO_3$ at $n = 5 \times 10^{21}$ cm^{-3} is shown in Fig. S10 (ESI†). At large n, the σ show a metallic-like drop with temperature consistent with degenerate semiconducting behaviour,

while the $|S|$ show a significant rise. For the p-type $LnCoO_3$ this results in a relatively flat temperature dependence of the PFs, with a shallow maximum around 500 K. For the n-type systems, on the other hand, the PFs rise with T up to 1000 K. At the smaller $n \approx 10^{21}$ cm^{-3} that maximises the PF, n-type STO shows similar behaviour at low T, but the increase flattens out above $\sim$600 K. Finally, the κ_{el} is proportional to both σ and T through eqn (23). For the p-type $LnCoO_3$, we predict a significant decrease from approx. 0.3 to 0.1 W m^{-1} K^{-1} between 200–1000 K, mirroring the behaviour of the σ, whereas for the n-type materials the two terms balance to yield a shallow temperature dependence. The κ_{el} of n-type STO shows intermediate behaviour, decreasing with T in line with the σ but maintaining a relatively high value of 0.4–0.6 W m^{-1} K^{-1}.

Experimental measurements on p-type $LnCoO_3$ typically show a large drop in S and increase in σ with temperature due to the thermal spin crossover from low-spin to high-spin Co^{3+}.[37,39,42–44] With reference to the electronic PDoS (Fig. 5 and Fig. S5/S6, ESI†), the spin crossover might be thought of as taking two electrons from the valence band and placing them in the conduction band, yielding two holes and two electrons per Co ion. With four Co ions per unit cell, this would correspond to a doping level of around 3.5×10^{22} cm^{-3}, which is well above the $\sim 5 \times 10^{21}$ cm^{-3} we predict would optimise the PF.

While crude, this picture is qualitatively supported by two observations. Firstly, extrapolating the data in Fig. 6, and considering the predicted temperature dependence in Fig. S10 (ESI†), suggests doping levels of this magnitude would yield p-type σ on the order of 100–1000 S cm^{-1} and $S < 100$ μV K^{-1}, which are broadly consistent with measurements performed above the spin-transition temperature.[36–39,42–44] Secondly, we might expect the large change in the (intrinsic) n through the transition to "swamp" a smaller extrinsic electron concentration, leading to a change in the sign of the Seebeck coefficient, which is seen in the measurements on n-type LCO in ref. 37 and 39.

On the other hand, comparison of the calculations to experimental measurements on p-type $LnCoO_3$[37,39,44] show that, at the n that match the S, the calculations consistently overestimate the σ by 1–2 orders of magnitude (Table S9, ESI†). This suggests the spin-crossover may also induce changes to the band structure that affect the electrical conductivity. For example, a flattening of the valence bands could increase the m^*_σ and/or increase the m^*_S, which would result in a lower σ/higher S for a given n. We defer a more detailed investigation of the effect of magnetic configuration on the electrical transport properties of the $LnCoO_3$ to a future study.

For present purposes, the comparison between our predictions for the low-spin $LnCoO_3$ and experimental measurements suggest the electrical properties could be significantly improved if the spin transition can be suppressed. Experimental evidence suggests this might be possible with certain material modifications, such as in $La(Mn_{1-x}Co_x)O_3$ solid solutions and $[LaCoO_3]_{1-x}[(La_{0.7}Sr_{0.3})CoO_3]_x$ composites.[37,44] The experiments in ref. 36 and 43 also show that the S is sensitive to the choice of Ln, which we speculate could be due to modulation of the spin transition temperature. More generally, the detremental impact of the spin transition, and the larger predicted $|S|$ of the low-spin $LnCoO_3$ compared to $SrTiO_3$, motivates the exploration of alternative perovskite chemistries, perhaps based on B-site M^{3+} ions without unpaired electrons and/or with stronger crystal-field splitting.

3.3 Thermoelectric figure of merit

Fig. 7 shows the predicted averaged p- and n-type figure of merit ZT of PCO as a function of n and T, and data for all three $LnCoO_3$ are provided in Fig. S11–S13 (ESI†). In general, the largest ZT are obtained at large n and high T, with the peak ZT at slightly lower n than the peak PFs due to the increase in the κ_{el} with n (*cf.* Fig. 6). We also predict considerably higher ZT for n-type doping than for p-type doping, due to the significantly higher PFs.

Considering the three heat-recovery scenarios set out in ref. 70, we predict maximum p-type ZT_{max} of 0.04–0.07 at 400 K,

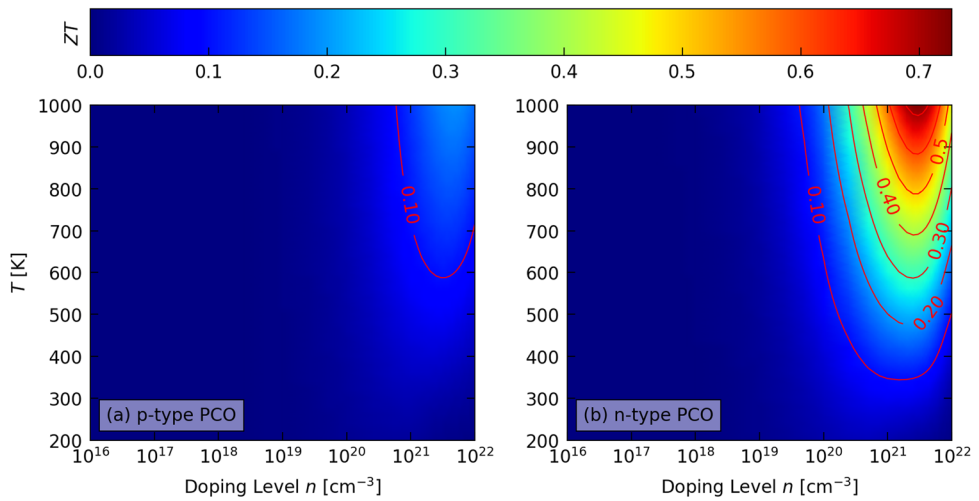

Fig. 7 Predicted average figure of merit ZT of $PrCoO_3$ (PCO) as a function of extrinsic carrier concentration n ("doping level") and temperature with (a) p-type and (b) n-type doping.

0.09–0.12 at 600 K and 0.17–0.19 at 1000 K (Table S10, ESI†). While these are considerably lower than the $ZT > 1$ required for commercial application,[2] they are also larger than the $ZT_{max} < 0.1$ reported in experiments on the $LnCoO_3$,[36,39,43,44] which highlights the scope for improved performance if the spin transition can be suppressed. Due to the significantly higher σ, we predict larger n-type ZT_{max} of 0.13–0.14, 0.28–0.31, and 0.66–0.73 at the three temperatures (Table S11, ESI†).

The ZT at 1000 K show modest anisotropy and vary by 7.5–15% around the averaged values (Fig. S11–S13, ESI†), due to a 5–25% variation in the PF and up to 10% variation in the κ_{latt}. The maximum ZT are generally obtained along the b direction, where the maximum PFs tend to align with the minimum κ_{latt}.

With the larger κ_{latt} predicted by including the contribution from intraband tunnelling, we predict $ZT_{max} = 0.06$, 0.14 and 0.31 for n-type STO at the three temperatures.[46] The latter value, and also the constituent properties of $S = -196$ μV K^{-1}, $\sigma = 258$ S cm^{-1} and $\kappa_{el} + \kappa_{latt} = 3.17$ W m^{-1} K^{-1}, are a very reasonable match to the range of values obtained in experiments around this temperature ($ZT = 0.27$–0.37, $S = -168$ to -233 μV K^{-1}, $\sigma = 200$–303 S cm^{-1}, $\kappa = 2.6$–3.1 W m^{-1} K^{-1}).[71–73]

The superior predicted performance of the n-type $LnCoO_3$ are due to lower a κ_{latt} and larger PFs, the latter predominantly from larger $|S|$, and also to larger σ at $T = 1000$ K. We predict the largest average n-type $ZT_{max} = 0.73$ at 1000 K for PCO, where the PF is $\sim$50% larger than predicted for STO.[46] However, while these predictions are promising, realising them requires that the spin transition can be suppressed with n-type doping. This has not been demonstrated experimentally, and may be challenging, or even impossible, to achieve in practice.

Finally, we note that the κ_{latt} is the majority contributor to the denominator in eqn (1) (Tables S10 and S11, ESI†), meaning that neglecting this contribution, as in the calculations in ref. 45, is a poor approximation. Indeed, the p-type ZT_{max} we predict are around 4× smaller than in ref. 45, and, given the relatively low ZT reported in experiments, we can confidently argue that the latter values are probably not realistic.

3.4 Discussion

In this study, we have applied an *ab initio* modelling workflow to investigate the thermoelectric performance of the lanthanide cobalates, $LaCoO_3$, $PrCoO_3$ and $NdCoO_3$. Compared to the more widely-studied titanate perovskites, in particular $SrTiO_3$, we predict the $LnCoO_3$ could potentially show lower intrinsic lattice thermal conductivity, larger Seebeck coefficients and, with heavy doping to optimise the electrical conductivity, higher power factors and thermoelectric figures of merit. By exploiting the microscopic insight available from the calculations, we have also established the origin of these differences and identified potential descriptors for favourable thermoelectric performance in oxide perovskites.

We first address the issue of the accuracy of our predictions relative to experimental measurements.

Our κ_{latt} are obtained by using the single-mode relaxation-time approximation to the phonon Boltzmann transport equation to obtain the particle-like conductivity, κ_p,[47] and by solving the Wigner transport equation to obtain the contribution from intraband tunnelling, κ_w.[48] The SM-RTA is an approximation to the full solution to the linearised Boltzmann transport equation. Moreover, the perturbative approach to determining the linewidths is based on the harmonic frequencies and eigenvectors, and does not take into account thermal expansion nor anharmonicity beyond third order (*e.g.* four-phonon scattering processes). Despite these shortcomings, comparison to experiments suggests this approach is accurate enough to reproduce experimental measurements with small errors. Of note, however, is the large κ_w predicted for both the lanthanide cobalate and the group II titanate perovskites, which indicates that amorphous-like heat conduction makes an important contribution to the κ_{latt} in these systems. It is likely that this may also be the case for other oxide perovskites, in which case this is an important general result.

The electrical transport properties are obtained by solving the electron Boltzmann transport equations within the rigid-band approximation, using approximate models for the electron scattering rates.[49,50] Calculations comparing the RBA to atomistic models of doped PbTe and HfCoSb, with n up to 4.5×10^{21} cm^{-3}, found 10–20% differences in the Seebeck coefficient.[74] In our previous work, we compared predictions for $SrTiO_3$ to measurements on heavily-doped single crystals ($n = 5 \times 10^{19}$–6.8×10^{20} cm^{-3}), and found a tendency for the calculations to over- and underestimate the electrical conductivity at low and high temperature, respectively, and to underestimate the $|S|$.[46,65] We also recently carried out a study where we used experimentally-measured relaxation times to predict the transport properties of STO, and found a similar tendency to underestimate the $|S|$ and overestimate the σ.[75] The models for electron scattering have been shown to work well across a wide range of systems, including the thermoelectrics SnS, SnSe, PbTe, Bi_2Te_3 and BiCuOSe and the hybrid halide perovskite $(CH_3NH_3)PbI_3$.[50] This approach also represents a significant conceptual improvement over using a fixed relaxation time.

We note that our predictions are for pristine single crystals, and do not take into account the impact of *e.g.* finite grain size and point defects on the transport properties.[76] In previous work on the bismuth oxychalcogenides, using a similar approach to the present study, we found that the calculations gave a near-quantitative reproduction of measurements on doped single crystals, but that experiments on consolidated powders showed much larger variability.[77]

In the context of the $LnCoO_3$ examined in the present work, the degradation of the $|S|$ through the spin crossover makes it difficult to quantitatively assess the accuracy of our predictions. Based on our previous studies on the titanate perovskites[46,75] we would expect the calculations to give reasonable "ballpark" predictions for the magnitude of the $|S|$, σ and PF, and of the n required to achieve them. As noted above, however, while several studies suggest it may be possible to control the spin transition chemically, at least to some extent,[37,43,44] it is not clear whether this can be achieved with the heavy doping required to optimise the (p- or n-type) electrical properties.

With this in mind, we close our discussion by highlighting the key features of the $LnCoO_3$ that the calculations predict

could lead to superior thermoelectric performance compared to STO. The first is that the $LnCoO_3$ show a significantly lower lattice lattice thermal conductivity, which, based on our analysis, can be attributed to weaker chemical bonding and lower phonon group velocities. This prediction is borne out in experiments,[43,44,65–67] and the good reproduction of high-temperature measurements in our calculations suggests the low κ_{latt} is not significantly impacted by the spin transition. A second key feature is the higher $|S|$, which we attribute to a larger Seebeck effective mass (*cf.* eqn (21)). In the $LnCoO_3$, this is partially offset by a high conductivity effective mass, and the p-type S are severely degraded in the high-spin magnetic configuration.[37,39,42–44] However, as a general observation, the possibility of superior electrical properties does motivate the exploration of a wider range of perovskite chemistries.

On this final point, modelling could be of considerable value in directing experiments towards the most promising candidates. In particular, the group-velocity metric κ_p/τ_{ph} in eqn (19) can be obtained from inexpensive harmonic phonon calculations, while the effective masses m_σ^*/m_S^* can be obtained from simple electronic-structure calculations using the CRTA.[69] One can therefore envisage a screening study using these metrics to prioritise candidate perovskites for further study, whether by more detailed theoretical modelling such as performed in the present work, or by experiments.

4 Conclusions

In summary, we have used an *ab initio* modelling workflow to obtain a comprehensive set of predictions for the thermoelectric properties and figure of merit of the orthorhombic low-spin lanthanide cobalate perovskites $LaCoO_3$, $PrCoO_3$ and $NdCoO_3$.

Compared to the more widely-studied titanate perovskites, and in particular $SrTiO_3$, we predict the $LnCoO_3$ to possess a beneficial lower lattice thermal conductivity, due to weaker chemical bonding and lower phonon group velocities. We find that glass-like intraband tunnelling makes a significant contribution to the κ_{latt} of both the $LnCoO_3$ and the titanate perovskites $CaTiO_3$ and STO, which may indicate that this heat-conduction mechanism is important in oxides more generally.

We predict the $LnCoO_3$ to have large carrier effective masses that result in high (absolute) Seebeck coefficients at the cost of reduced electrical conductivity, the latter of which requires heavier doping to offset. A combination of higher conductivity masses and stronger carrier scattering result in poor p-type conductivity, whereas the high $|S|$ and reasonable conductivity predicted for the n-type $LnCoO_3$ could yield superior power factors to STO if carrier concentrations on the order of $\sim 5 \times 10^{21}$ cm^{-3} can be obtained. However, comparison to experiments suggests the electrical properties are negatively impacted by the thermally-activated transition from low- to high-spin Co^{3+}, and that this behaviour may make it difficult or impossible to retain dominant n-type transport at elevated temperature.

If the spin transition can be suppressed, we predict modest p- and n-type ZT of up to 0.19 and 0.73 at 1000 K, the latter of which is competitive with other oxide materials. Although it is unclear whether these ZT can be achieved in practice, our results strongly motivate the exploration of alternative oxide perovskites, and we identify two descriptors, calculated from the harmonic phonon spectra and electronic structure, that could be used as a basis for this.

Author contributions

Conceptualization, methodology and writing – all authors; data curation, formal analysis and investigation – AZK and JMF; funding acquisition – JMS; software, project administration and supervision – JMF and JMS; resources – JMS.

Data availability

Data will be made available after publication in an online repository at **https://doi.org/10.17632/trx37mt89j**. Our analysis code is available on GitHub at **https://github.com/skelton-group/ZT-Calc-Workflow**.

Conflicts of interest

There are no conflicts to declare.

Acknowledgements

AZK is supported by a University of Manchester PhD studentship, and JMF and JMS are supported by a UK Research and Innovation (UKRI) Future Leaders Fellowship (MR/T043121/1, MR/Y033973/1). The calculations used the ARCHER 2 HPC facility *via* the UK Materials Chemistry Consortium, which is funded by the UK Engineering and Physical Sciences Research Council (EP/R029431, EP/X035859).

Notes and references

1 A. Firth, B. Zhang and A. Yang, *Appl. Energy*, 2019, **235**, 1314–1334.
2 R. Freer and A. V. Powell, *J. Mater. Chem. C*, 2020, **8**, 441–463.
3 G. Tan, L.-D. Zhao and M. G. Kanatzidis, *Chem. Rev.*, 2016, **116**, 12123–12149.
4 S. K. Guillemot, A. Suwardi, N. Kaltsoyannis and J. M. Skelton, *J. Mater. Chem. A*, 2024, **12**, 2932–2948.
5 A. Walsh, D. J. Payne, R. G. Egdell and G. W. Watson, *Chem. Soc. Rev.*, 2011, **40**, 4455–4463.
6 C. Li, J. Hong, A. May, D. Bansal, S. Chi, T. Hong, G. Ehlers and O. Delaire, *Nat. Phys.*, 2015, **11**, 1063–1069.
7 R. Deng, X. Su, Z. Zheng, W. Liu, Y. Yan, Q. Zhang, V. P. Dravid, C. Uher, M. G. Kanatzidis and X. Tang, *Sci. Adv.*, 2018, **4**, eaar5606.
8 H. Lee, T. Kim, S. C. Son, J. Kim, D. Kim, J. Lee and I. Chung, *Mater. Today Phys.*, 2023, **31**, 100986.

9 B. Zhu, X. Liu, Q. Wang, Y. Qiu, Z. Shu, Z. Guo, Y. Tong, J. Cui, M. Gu and J. He, *Energy Environ. Sci.*, 2020, **13**, 2106–2114.
10 K. Biswas, J. He, I. D. Blum, C.-I. Wu, T. P. Hogan, D. N. Seidman, V. P. Dravid and M. G. Kanatzidis, *Nature*, 2012, **489**, 414–418.
11 G. Tan, F. Shi, S. Hao, L.-D. Zhao, H. Chi, X. Zhang, C. Uher, C. Wolverton, V. P. Dravid and M. G. Kanatzidis, *Nat. Commun.*, 2016, **7**, 12167.
12 C. Zhou, Y. K. Lee, Y. Yu, S. Byun, Z.-Z. Luo, H. Lee, B. Ge, Y.-L. Lee, X. Chen, J. Y. Lee, O. Cojocaru-Mirédin, H. Chang, J. Im, S.-P. Cho, M. Wuttig, V. P. Dravid, M. G. Kanatzidis and I. Chung, *Nat. Mater.*, 2021, **20**, 1378–1384.
13 T. Kim, H. Lee and I. Chung, *Bull. Korean Chem. Soc.*, 2024, **45**, 186–199.
14 S. Byun, B. Ge, H. Song, S.-P. Cho, M. S. Hong, J. Im and I. Chung, *Joule*, 2024, **8**, 1520–1538.
15 C. Jiang, X. Fan, B. Feng, J. Hu, Q. Xiang, G. Li, Y. Li and Z. He, *J. Alloys Compd.*, 2017, **692**, 885–891.
16 Y. Zheng, X. Y. Tan, X. Wan, X. Cheng, Z. Liu and Q. Yan, *ACS Appl. Energy Mater.*, 2020, **3**, 2078–2089.
17 R. Freer, D. Ekren, T. Ghosh, K. Biswas, P. Qiu, S. Wan, L. Chen, S. Han, C. Fu, T. Zhu, A. K. M. A. Shawon, A. Zevalkink, K. Imasato, G. J. Snyder, M. Ozen, K. Saglik, U. Aydemir, R. Cardoso-Gil, E. Svanidze, R. Funahashi, A. V. Powell, S. Mukherjee, S. Tippireddy, P. Vaqueiro, F. Gascoin, T. Kyratsi, P. Sauerschnig and T. Mori, *J. Phys. Energy*, 2022, **4**, 022002.
18 I. Terasaki, Y. Sasago and K. Uchinokura, *Phys. Rev. B: Condens. Matter Mater. Phys.*, 1997, **56**, R12685–R12687.
19 H. Yakabe, K. Kikuchi, I. Terasaki, Y. Sasago and K. Uchinokura, *Proceedings of the 1997 16th International Conference on Thermoelectrics*, 1997, pp. 523–527.
20 W. Koshibae, K. Tsutsui and S. Maekawa, *Phys. Rev. B: Condens. Matter Mater. Phys.*, 2000, **62**, 6869–6872.
21 M. Ito and D. Furumoto, *J. Alloys Compd.*, 2008, **450**, 517–520.
22 Y. Miyazaki, *Solid State Ionics*, 2004, **172**, 463–467.
23 M. Shikano and R. Funahashi, *Appl. Phys. Lett.*, 2003, **82**, 1851–1853.
24 S. Saini, H. S. Yaddanapudi, K. Tian, Y. Yin, D. Magginetti and A. Tiwari, *Sci. Rep.*, 2017, **7**, 44621.
25 R. Funahashi, I. Matsubara and S. Sodeoka, *Appl. Phys. Lett.*, 2000, **76**, 2385–2387.
26 S. Wang, Z. Bai, H. Wang, Q. Lü, J. Wang and G. Fu, *J. Alloys Compd.*, 2013, **554**, 254–257.
27 T. Tsubota, M. Ohtaki, K. Eguchi and H. Arai, *J. Mater. Chem.*, 1997, **7**, 85–90.
28 M. Ohtaki, K. Araki and K. Yamamoto, *J. Electron. Mater.*, 2009, **38**, 1234–1238.
29 T. Okuda, K. Nakanishi, S. Miyasaka and Y. Tokura, *Phys. Rev. B: Condens. Matter Mater. Phys.*, 2001, **63**, 113104.
30 H. Muta, K. Kurosaki and S. Yamanaka, *J. Alloys Compd.*, 2003, **350**, 292–295.
31 H. Muta, K. Kurosaki and S. Yamanaka, *J. Alloys Compd.*, 2005, **392**, 306–309.
32 J. Wang, B.-Y. Zhang, H.-J. Kang, Y. Li, X. Yaer, J.-F. Li, Q. Tan, S. Zhang, G.-H. Fan, C.-Y. Liu, L. Miao, D. Nan, T.-M. Wang and L.-D. Zhao, *Nano Energy*, 2017, **35**, 387–395.
33 T. Kobayashi, H. Takizawa, T. Endo, T. Sato, M. Shimada, H. Taguchi and M. Nagao, *J. Solid State Chem.*, 1991, **92**, 116–129.
34 D. Flahaut, T. Mihara, R. Funahashi, N. Nabeshima, K. Lee, H. Ohta and K. Koumoto, *J. Appl. Phys.*, 2006, **100**, 084911.
35 X. Song, S. A. Paredes Navia, L. Liang, C. Boyle, C.-O. Romo-De-La-Cruz, B. Jackson, A. Hinerman, M. Wilt, J. Prucz and Y. Chen, *ACS Appl. Mater. Interfaces*, 2018, **10**, 39018–39024.
36 J.-W. Moon, Y. Masuda, W.-S. Seo and K. Koumoto, *Mater. Sci. Eng., B*, 2001, **85**, 70–75.
37 C. Autret, J. Hejtmánek, K. Knížek, M. Maryško, Z. Jirák, M. Dlouhá and S. Vratislav, *J. Phys.: Condens. Matter*, 2005, **17**, 1601.
38 V. Dudnikov, A. Fedorov, Y. Orlov, L. Solovyov, S. Vereshchagin, S. Y. Gavrilkin, A. Y. Tsvetkov, M. Gorev, S. Novikov and S. Ovchinnikov, *Ceram. Int.*, 2020, **46**, 17987–17991.
39 V. A. Dudnikov, Y. S. Orlov, L. A. Solovyov, S. N. Vereshchagin, Y. N. Ustyuzhanin, S. M. Zharkov, G. M. Zeer, A. A. Borus, V. S. Bondarev and S. G. Ovchinnikov, *J. Taiwan Inst. Chem. Eng.*, 2024, **162**, 105560.
40 J. A. Alonso, M. J. Martínez-Lope, C. de la Calle and V. Pomjakushin, *J. Mater. Chem.*, 2006, **16**, 1555–1560.
41 K. Knížek, J. C. V. Hejtmánek, Z. C. V. Jirák, P. Tomeš, P. Henry and G. André, *Phys. Rev. B: Condens. Matter Mater. Phys.*, 2009, **79**, 134103.
42 J.-Q. Yan, J.-S. Zhou and J. B. Goodenough, *Phys. Rev. B: Condens. Matter Mater. Phys.*, 2004, **69**, 134409.
43 H. Hashimoto, T. Kusunose and T. Sekino, *J. Alloys Compd.*, 2009, **484**, 246–248.
44 A. Kumar, D. Sivaprahasam and A. D. Thakur, *Mater. Chem. Phys.*, 2021, **269**, 124750.
45 H. Absike, N. Baaalla, L. Attou, H. Labrim, B. Hartiti and H. Ez-zahraouy, *Solid State Commun.*, 2022, **345**, 114684.
46 A. Z. Khan, J. M. Flitcroft and J. M. Skelton, *Mater. Adv.*, 2024, **5**, 652–664.
47 A. Togo, L. Chaput and I. Tanaka, *Phys. Rev. B: Condens. Matter Mater. Phys.*, 2015, **91**, 094306.
48 M. Simoncelli, N. Marzari and F. Mauri, *Phys. Rev. X*, 2022, **12**, 041011.
49 G. K. Madsen, J. Carrete and M. J. Verstraete, *Comput. Phys. Commun.*, 2018, **231**, 140–145.
50 A. M. Ganose, J. Park, A. Faghaninia, R. Woods-Robinson, K. A. Persson and A. Jain, *Nat. Commun.*, 2021, **12**, 2222.
51 G. Kresse and J. Hafner, *Phys. Rev. B: Condens. Matter Mater. Phys.*, 1993, **47**, 558–561.
52 A. Jain, S. P. Ong, G. Hautier, W. Chen, W. D. Richards, S. Dacek, S. Cholia, D. Gunter, D. Skinner, G. Ceder and K. A. Persson, *APL Mater.*, 2013, **1**, 011002.
53 J. P. Perdew, A. Ruzsinszky, G. I. Csonka, O. A. Vydrov, G. E. Scuseria, L. A. Constantin, X. Zhou and K. Burke, *Phys. Rev. Lett.*, 2008, **100**, 136406.
54 P. E. Blöchl, *Phys. Rev. B: Condens. Matter Mater. Phys.*, 1994, **50**, 17953–17979.
55 G. Kresse and D. Joubert, *Phys. Rev. B: Condens. Matter Mater. Phys.*, 1999, **59**, 1758–1775.
56 H. J. Monkhorst and J. D. Pack, *Phys. Rev. B: Condens. Matter Mater. Phys.*, 1976, **13**, 5188–5192.

57 A. Togo and I. Tanaka, *Scr. Mater.*, 2015, **108**, 1–5.
58 X. Gonze and C. Lee, *Phys. Rev. B: Condens. Matter Mater. Phys.*, 1997, **55**, 10355–10368.
59 M. Gajdoš, K. Hummer, G. Kresse, J. Furthmüller and F. Bechstedt, *Phys. Rev. B: Condens. Matter Mater. Phys.*, 2006, **73**, 045112.
60 A. V. Krukau, O. A. Vydrov, A. F. Izmaylov and G. E. Scuseria, *J. Chem. Phys.*, 2006, **125**, 224106.
61 A. M. Ganose, A. J. Jackson and D. O. Scanlon, *J. Open Source Software*, 2018, **3**, 717.
62 J. M. Skelton, D. S. D. Gunn, S. Metz and S. C. Parker, *J. Chem. Theory Comput.*, 2020, **16**, 3543–3557.
63 K. Momma and F. Izumi, *J. Appl. Crystallogr.*, 2011, **44**, 1272–1276.
64 J. Li, Y. Wang, X. Yang, H. Kang, Z. Cao, X. Jiang, Z. Chen, E. Guo and T. Wang, *Chem. Eng. J.*, 2022, **428**, 131121.
65 S. Ohta, T. Nomura, H. Ohta and K. Koumoto, *J. Appl. Phys.*, 2005, **97**, 034106.
66 A. J. Ahmed, S. M. K. Nazrul Islam, R. Hossain, J. Kim, M. Kim, M. Billah, M. S. A. Hossain, Y. Yamauchi and X. Wang, *R. Soc. Open Sci.*, 2019, **6**, 190870.
67 S. P. Singh, N. Kanas, T. D. Desissa, M. Johnsson, M.-A. Einarsrud, T. Norby and K. Wiik, *J. Eur. Ceram. Soc.*, 2020, **40**, 401–407.
68 G. Tan, L.-D. Zhao and M. G. Kanatzidis, *Chem. Rev.*, 2016, **116**, 12123–12149.
69 Z. M. Gibbs, F. Ricci, G. Li, H. Zhu, K. Persson, G. Ceder, G. Hautier, A. Jain and G. J. Snyder, *npj Comput. Mater.*, 2017, **3**, 8.
70 S. LeBlanc, S. K. Yee, M. L. Scullin, C. Dames and K. E. Goodson, *Renewable Sustainable Energy Rev.*, 2014, **32**, 313–327.
71 A. Kikuchi, N. Okinaka and T. Akiyama, *Scr. Mater.*, 2010, **63**, 407–410.
72 H. Wang, C. Wang, W. Su, J. Liu, Y. Zhao, H. Peng, J. Zhang, M. Zhao, J. Li, N. Yin and L. Mei, *Mater. Res. Bull.*, 2010, **45**, 809–812.
73 D. Srivastava, C. Norman, F. Azough, M. C. Schäfer, E. Guilmeau, D. Kepaptsoglou, Q. M. Ramasse, G. Nicotra and R. Freer, *Phys. Chem. Chem. Phys.*, 2016, **18**, 26475–26486.
74 M.-S. Lee and S. D. Mahanti, *Phys. Rev. B: Condens. Matter Mater. Phys.*, 2012, **85**, 165149.
75 Y. Zhu, J. M. Skelton, D. J. Lewis and R. Freer, *JPhys Energy*, 2024, **6**, 025027.
76 D. Narducci, E. Selezneva, G. Cerofolini, S. Frabboni and G. Ottaviani, *J. Solid State Chem.*, 2012, **193**, 19–25.
77 J. M. Flitcroft, A. Althubiani and J. M. Skelton, *JPhys Energy*, 2024, **6**, 025011.

